

The daily modulations and broadband strategy in axion searches. An application with CAST-CAPP detector

C. M. Adair,¹ K. Altenmüller,² V. Anastassopoulos,³ S. Arguedas Cuendis,⁴ J. Baier,⁵ K. Barth,⁴ A. Belov,⁶ D. Bozicevic,⁷ H. Bräuninger,^{8,*} G. Cantatore,^{9,10} F. Caspers,^{4,11} J. F. Castel,² S. A. Çetin,¹² W. Chung,¹³ H. Choi,¹⁴ J. Choi,¹³ T. Dafni,² M. Davenport,⁴ A. Dermenev,⁶ K. Desch,¹⁵ B. Döbrich,¹⁶ H. Fischer,⁵ W. Funk,⁴ J. Galan,² A. Gardikiotis,¹⁷ S. Gninenko,⁶ J. Golm,^{4,18} M. D. Hasinoff,¹ D. H. H. Hoffmann,¹⁹ D. Díez Ibáñez,² I. G. Irastorza,² K. Jakovčić,²⁰ J. Kaminski,¹⁵ M. Karuza,^{9,21,22} C. Krieger,²³ Ç. Kutlu,^{13,14} B. Lakić,^{20,*} J. M. Laurent,⁴ J. Lee,¹⁴ S. Lee,¹³ G. Luzón,² C. Margalejo,² M. Maroudas,^{23,†} L. Miceli,¹³ H. Mirallas,² L. Obis,² A. Özbey,²⁴ K. Özbozduman,^{25,‡} M. J. Pivovarov,²⁶ M. Rosu,²⁷ J. Ruz,²⁶ E. Ruiz-Chóliz,²⁸ S. Schmidt,¹⁵ Y. K. Semertzidis,^{13,14} S. K. Solanki,²⁹ L. Stewart,⁴ I. Tsagris,³ T. Vafeiadis,⁴ J. K. Vogel,^{2,26} M. Vretenar,²¹ S. Youn,¹³ A. Zhitnitsky,^{1,§} and K. Zioutas^{3,4}

¹*Department of Physics and Astronomy, University of British Columbia, V6T 1Z1 Vancouver, Canada*

²*Centro de Astropartículas y Física de Altas Energías (CAPA),
Universidad de Zaragoza, 50009 Zaragoza, Spain*

³*Physics Department, University of Patras, 26504 Patras, Greece*

⁴*European Organization for Nuclear Research (CERN), CH-1211 Genève, Switzerland*

⁵*Physikalisches Institut, Albert-Ludwigs-Universität Freiburg, 79104 Freiburg, Germany*

⁶*Author affiliated with an institute covered by a cooperation agreement with CERN*

⁷*University of Rijeka, Faculty of Engineering, 51000 Rijeka, Croatia*

⁸*Max-Planck-Institut für Extraterrestrische Physik, D-85741 Garching, Germany*

⁹*Istituto Nazionale di Fisica Nucleare (INFN), Sezione di Trieste, 34127 Trieste, Italy*

¹⁰*Università di Trieste, 34127 Trieste, Italy*

¹¹*European Scientific Institute (ESI), 74160 Archamps, France*

¹²*Istinye University, Department of Basic Sciences, 34396 Sariyer, Istanbul, Türkiye*

¹³*Center for Axion and Precision Physics Research,
Institute for Basic Science (IBS), Daejeon 34141, Republic of Korea*

¹⁴*Department of Physics, Korea Advanced Institute of Science and Technology (KAIST), Daejeon 34141, Republic of Korea*

¹⁵*Physikalisches Institut, University of Bonn, 53115 Bonn, Germany*

¹⁶*Max-Planck-Institut für Physik (Werner-Heisenberg-Institut),
Boltzmannstr. 8, 85748 Garching bei München, Germany*

¹⁷*Istituto Nazionale di Fisica Nucleare (INFN), Sezione di Padova, 35131 Padova, Italy*

¹⁸*Institute for Optics and Quantum Electronics, Friedrich Schiller University Jena, 07743 Jena, Germany*

¹⁹*Xi'An Jiaotong University, School of Science, Xi'An, 710049, China*

²⁰*Rudjer Bošković Institute, 10000 Zagreb, Croatia*

²¹*University of Rijeka, Faculty of Physics, 51000 Rijeka, Croatia*

²²*University of Rijeka, Photonics and Quantum Optics Unit,
Center of Excellence for Advanced Materials and Sensing Devices,*

and Centre for Micro and Nano Sciences and Technologies, 51000 Rijeka, Croatia

²³*Institute of Experimental Physics, University of Hamburg, 22761 Hamburg, Germany*

²⁴*Department of Mechanical Engineering, Istanbul University-Cerrahpaşa, Istanbul, Türkiye*

²⁵*Bogazici University, Physics Department, 34342 Bebek, Istanbul, Türkiye*

²⁶*Lawrence Livermore National Laboratory, Livermore, CA 94550, USA*

²⁷*Extreme Light Infrastructure - Nuclear Physics (ELI-NP), 077125 Magurele, Romania*

²⁸*Institut für Physik, Johannes Gutenberg Universität Mainz, 55128 Mainz, Germany*

²⁹*Max-Planck-Institut für Sonnensystemforschung, 37077 Göttingen, Germany*

(Dated: May 21, 2024)

It has been previously advocated that the presence of the daily and annual modulations of the axion flux on the Earth's surface may dramatically change the strategy of the axion searches. The arguments were based on the so-called Axion Quark Nugget (AQN) dark matter model which was originally put forward to explain the similarity of the dark and visible cosmological matter densities $\Omega_{\text{dark}} \sim \Omega_{\text{visible}}$. In this framework, the population of galactic axions with mass $10^{-6}\text{eV} \lesssim m_a \lesssim 10^{-3}\text{eV}$ and velocity $\langle v_a \rangle \sim 10^{-3}c$ will be accompanied by axions with typical velocities $\langle v_a \rangle \sim 0.6c$ emitted by AQNs. Furthermore, in this framework, it has also been argued that the AQN-induced axion daily modulation (in contrast with the conventional WIMP paradigm) could be as large as (10 – 20)%, which represents the main motivation for the present investigation. We argue that the daily modulations along with the broadband detection strategy can be very useful tools for the discovery of such relativistic axions. The data from the CAST-CAPP detector have been used following such arguments. Unfortunately, due to the dependence of the amplifier chain on temperature-dependent gain drifts and other factors, we could not conclusively show the presence

or absence of a dark sector-originated daily modulation. However, this proof of principle analysis procedure can serve as a reference for future studies.

I. INTRODUCTION AND MOTIVATION

The Peccei-Quinn mechanism, accompanied by axions, remains the most compelling resolution of the strong \mathcal{CP} problem; see original papers [1–7] and recent reviews [8–18]. The conventional idea for the production of the dark matter (DM) axions is either by the misalignment mechanism when the cosmological field $\theta(t)$ oscillates and emits cold axions before it settles at a minimum, or via the decay of topological objects, see recent reviews [8–18]. In both cases, the resulting axion is non-relativistic with typical velocities $\langle v_a \rangle \sim 10^{-3}c$.

In addition to these well-established mechanisms, a fundamentally novel mechanism for axion production was studied in recent papers [19–23]. This mechanism is rooted in the so-called axion quark nugget (AQN) DM model [24], which will be briefly reviewed in Sect. II. For this introduction, we just need to make several short comments on this model. First, the AQN construction in many respects is similar to the original quark-nugget model suggested by Witten [25]. This type of DM is “cosmologically dark” not because of the weakness of the AQN interactions, but due to their small cross-section-to-mass ratio, which scales down many observable consequences of an otherwise strongly-interacting DM candidate, see Sect. II for more details. The second, and most important feature for this work, is that the AQNs will emit relativistic axions $\langle v_a \rangle \sim 0.6c$ in contrast with conventional mechanisms mentioned above where the axions assume typical galactic velocities $\langle v_a \rangle \sim 10^{-3}c$, see Sect. III for details.

This distinct feature dramatically changes the entire axion detection strategy as it must be a broadband search. Many new elements can be implemented in such broadband searches, such as analysis for the daily modulation, see Sect. IV for details.

The production of the relativistic axions has been discussed in the literature, outside the AQN framework, see [26] where several mechanisms for the production of the relativistic axions had been proposed and coined as the CaB (cosmic axion background). In this sense, our proposal for broadband searches has much more generic applicability, not limited to the AQN model.

However, there are a few differences between the AQN-induced axions and the mechanisms of production of the CaB axions considered in [26]. The AQN-induced axions are produced when an AQN interacts with the Earth’s material, and therefore, are mostly localized on

the Earth’s (or other stars or planets) surface, while the axions considered in [26] are cosmological in nature, and distributed uniformly in the Universe. As a result, the dominant portion of the relativistic axions (which is the topic of the present work) should be related to the AQN-induced events with a well-defined estimate for the axion density on the Earth’s surface as reviewed in Sect. III.

The most distinct feature relevant to the present study, however, is as follows. The study of the daily modulations of the axions produced by the CaB mechanism considered in [26] requires the detector to be sensitive to the directionality.

The daily modulations emerge due to the change in the relative orientation of the Earth’s axis of rotation with respect to the galactic wind. If an instrument is sensitive to the directionality then the daily modulations can be studied by such an instrument.

The daily modulations of the relativistic axions can be, in principle, studied (though not very efficiently) by the presently available instruments which were not originally designed to measure directionality. In fact, the recent analysis [27] uses ADMX data to study the daily modulations due to CaB. For the AQN-induced axions, in addition to this effect, there will be an extra contribution to the daily modulations that emerges as a result of the difference in mass (size) of the AQNs when they enter or exit Earth as we discuss in Sect. III. Therefore, even if the instrument is not sensitive to the directionality it will be still capable of studying the daily modulations as a result of the asymmetry between AQNs entering and exiting the Earth’s surface as discussed in Sect. III.

We expect that the density of the AQN-induced axions on the Earth’s surface should be much larger than the density of the CaB axions being constrained by the CMB photon density, see Sect. III with the estimates. As a result, we expect that the time modulation effects, which is the topic of the present studies will be dominated by the AQN-induced axions¹

There is another feature of the AQN-induced axions that is not shared by the CaB mechanisms considered in [26]. The AQNs are very massive objects. Therefore, the AQN flux on Earth is highly non-uniform, in contrast with conventional DM models, and in contrast with CaB flux. As a result of this aspect, there will be some “local

* deceased

† marios.maroudas@cern.ch

‡ kaan.ozbozduman@cern.ch

§ arz@phas.ubc.ca

¹ There is an enhancement factor such as the modification of the local density of DM particles close to the Earth’s surface. The corresponding enhancement factor of the DM density is translated into a corresponding significant modification of the AQN-induced density of the relativistic axions on the Earth’s surface. This effect is very important for the AQN-induced axions and completely irrelevant for CaB axions as the cosmic relativistic axions are not related to the DM density and cannot be trapped by the Earth’s gravitational field.

flashes” which may enhance by several orders of magnitude the axion count for a short period of time, see Sect. III with details. It happens when the AQN hits the Earth’s surface in the vicinity (100 km or less) of the detector, see next Sect. II with specific estimates.

Our presentation is organized as follows. In the next Sect. II we briefly overview the basic ideas of the AQN framework. In Sect. III and IV we overview the main characteristics of the AQN-induced axions relevant to the present work, including their spectrum and the intensity on the Earth’s surface. Sect. V is devoted to our estimations for the daily modulation, including analysis of possible tests to discriminate the genuine signal from spurious signals and noise. In Sect. VI we apply all these generic features of the broadband analysis to study possible daily modulations by using the previously recorded CAST-CAPP dataset. We then conclude with Sect. VII providing some suggestions for future studies.

II. THE AQN DARK MATTER MODEL. THE BASICS

The AQN construction in many respects is similar to Witten’s quark nuggets, see [25, 28, 29]. This type of DM is “cosmologically dark” as a result of the smallness of the parameter relevant for cosmology, which is the cross-section-to-mass ratio of the DM particles. This numerically small ratio scales down many observable consequences of an otherwise strongly-interacting DM candidate in the form of the AQN nuggets.

There are several additional elements in the AQN model in comparison with the older well-known and well-studied theoretical constructions [25, 28, 29]. First, there is an additional stabilization factor for the nuggets provided by the axion domain walls which are copiously produced during the QCD transition. This additional element helps to alleviate a number of problems with Witten’s original model². Secondly, the nuggets can be

² In particular, a first-order phase transition is not a required feature for nugget formation as the axion domain wall (with internal QCD substructure) plays the role of the squeezer. Another problem of the old construction [25, 28, 29] is that nuggets likely evaporate on the Hubble time scale. For the AQN model, this is not the case because the vacuum-ground-state energies inside (the color-superconducting phase) and outside the nugget (the hadronic phase) are drastically different. Therefore, these two systems can coexist only in the presence of an external pressure, provided by the axion domain wall. This should be contrasted with the original model [25, 28, 29], which is assumed to be stable at zero external pressure.

This difference has major observational consequences- the Witten’s nugget will turn a neutron star (NS) into a quark star if it hits the NS. In contrast, a matter type AQN will not turn an entire star into a new quark phase because the quark matter in the AQNs is supported by external axion domain wall pressure, and therefore, can be extended only to relatively small distance $\sim m_a^{-1}$, which is much shorter than the NS size.

made of *matter* as well as *antimatter* during the QCD transition.

The presence of antimatter nuggets in the AQN framework is an inevitable and direct consequence of the \mathcal{CP} violating axion field which is present in the system during the QCD time. As a result of this feature the DM density, Ω_{DM} , and the visible density, Ω_{visible} , will automatically assume the same order of magnitude densities $\Omega_{\text{DM}} \sim \Omega_{\text{visible}}$ irrespectively to the parameters of the model, such as the axion mass m_a . This feature represents a generic property of the construction [24] as both components, the visible, and the dark are proportional to the same fundamental dimensional constant of the theory, the Λ_{QCD} .

We refer to the original papers [36–39] devoted to the specific questions related to the nugget’s formation, generation of the baryon asymmetry, and survival pattern of the nuggets during the evolution in early Universe with its unfriendly environment. We also refer to a recent brief review article [30] which explains several subtle points on the formation mechanism, and survival pattern of the AQNs during the early stages of the evolution, including the Cosmic Microwave Background (CMB) Big Bang Nucleosynthesis (BBN), and recombination epochs.

In this work we take the agnostic viewpoint and assume that such nuggets made of *antimatter* are present in our Universe today and they were present at earlier times, irrespectively of their formation mechanism. This assumption is consistent with all presently available cosmological, astrophysical, and terrestrial constraints as long as the average baryon charge of the nuggets is sufficiently large as we review below.

The strongest direct detection limit³ is set by the Ice-Cube Observatory’s, see Appendix A in [21]:

$$\langle B \rangle > 3 \cdot 10^{24} \quad [\text{direct (non)detection constraint}]. \quad (1)$$

Similar limits are also obtainable from the ANITA and from geothermal constraints which are also consistent with Eq. 1 as estimated in [41].

The authors of Ref. [33] considered a generic constraint for the nuggets made of antimatter (ignoring all essential specifics of the AQN model such as quark matter CS phase of the nugget’s core). Our constraints (Eq. 1) are consistent with their findings including the CMB and BBN, and others, except the constraints derived from the so-called “Human Detectors”. As explained in [42] the corresponding estimates of Ref. [33] are oversimplified and do not have the same status as those derived from CMB or BBN constraints.

We now present the rate at which AQNs hit the Earth assuming the local DM density of $\rho_{\text{DM}} \simeq 0.3 \text{ GeVcm}^{-3}$.

³ Non-detection of etching tracks in ancient mica gives another indirect constraint on the flux of DM nuggets with mass $M > 55\text{g}$ [40]. This constraint is based on the assumption that all nuggets have the same mass, which is not the case for the AQN model.

Property	Typical value or feature
AQN's mass [M_N]	$M_N \approx 16 g (B/10^{25})$ [30]
baryon charge constraints [B]	$B \geq 3 \cdot 10^{24}$ [30]
annihilation cross section [σ]	$\sigma \approx \kappa\pi R^2 \simeq 1.5 \cdot 10^{-9} \text{cm}^2 \cdot \kappa (R/2.2 \cdot 10^{-5} \text{cm})^2$
density of AQNs [n_{AQN}]	$n_{\text{AQN}} \sim 0.3 \cdot 10^{-25} \text{cm}^{-3} (10^{25}/B)$ [30]
survival pattern during BBN	$\Delta B/B \ll 1$ [31–34]
survival pattern during CMB	$\Delta B/B \ll 1$ [31, 33, 35]
survival pattern during post-recombination	$\Delta B/B \ll 1$ [36]

TABLE I. Basic properties of the AQNs

Assuming the conventional halo model, one arrives at [21]:

$$\begin{aligned} \frac{\langle \dot{N} \rangle}{4\pi R_\oplus^2} &\simeq \frac{4 \cdot 10^{-2}}{\text{km}^2 \text{ yr}} \left(\frac{\rho_{\text{DM}}}{0.3 \frac{\text{GeV}}{\text{cm}^3}} \right) \left(\frac{\langle v_{\text{AQN}} \rangle}{220 \frac{\text{km}}{\text{s}}} \right) \left(\frac{10^{25}}{\langle B \rangle} \right), \\ \langle \dot{N} \rangle &\simeq 0.67 \text{ s}^{-1} \left(\frac{10^{25}}{\langle B \rangle} \right) \simeq 2.1 \cdot 10^7 \text{ yr}^{-1} \left(\frac{10^{25}}{\langle B \rangle} \right) \end{aligned} \quad (2)$$

In obtaining Eq. 2 it was assumed that $\langle \dot{N} \rangle \approx 4\pi b^2 n_{\text{AQN}} v_{\text{AQN}}$, where $b \approx 1.0013 R_\oplus$ is the impact parameter for Earth, and we averaged over incident angles of impacting AQNs, see Appendix C in [21] with details. We also assume that the AQNs represent the dominant portion of the DM. Numerical expressions for Eq. 2 were derived in [21] using full-scale Monte Carlo simulations which account for all types of AQN trajectories with different AQN masses $M_N \simeq m_p |B|$, different incident angles, different initial velocities and size distributions. It was shown that none of these factors significantly affect our estimate. The result in Eq. 2 suggests that AQNs with a typical size $B \approx 10^{25}$ hit the Earth's surface with a frequency on the order of once a day (i.e., hundreds per year) per $100 \times 100 \text{ km}^2$.

We conclude this brief review subsection with Tab. I which summarizes the basic features and parameters of the AQNs. The parameter κ in Tab. I is introduced to account for the fact that not all matter striking the nugget will annihilate and not all of the energy released by annihilation will be thermalized in the nuggets. The ratio $\Delta B/B \ll 1$ in the Table implies that only a small portion ΔB of the total (anti)baryon charge B hidden in form of the AQNs get annihilated during big-bang nucleosynthesis (BBN), Cosmic Microwave Background (CMB), or post-recombination epochs (including the galaxy and star formation), while the dominant portion of the baryon charge survives until the present time. Independent analysis [34] and [33] also support our original claims, as cited in Tab. I, that the anti-quark nuggets survive the BBN and CMB epochs.

Finally, one should mention here that the AQN model with the same set of parameters may explain several other puzzling observations in different environments. In particular, it may explain the primordial Li puzzle [32] during the early Universe evolution. On a different, galactic scale, it may explain the observed excess of the UV radiation [43]. The excess of radiation is observed in many

different frequency bands, from UV to optical, IR, and even radio frequency bands. It is normally expressed as excess in the Extra-galactic Background Light (EBL), see e.g. review [44]. The energy injection due to the AQN-induced processes may explain a portion or even entire observed excesses in different frequency bands.

It may also explain some observed inconsistencies on small galactic scales (such as the Core-Cusp problem [45, 46], the Too-Big-to-Fail problem [47], etc) which are hard to explain within the conventional CDM paradigm [48]. It may also shed some light on the long-standing solar corona heating problem [49, 50], which could be the manifestation of the AQN's processes at different scales (outside of the galactic scale where the DM is expected to manifest itself). Finally, the AQNs may also explain some mysterious events observed on the Earth scale, such as the anomalous events recorded by ANITA [51].

III. THE AQN-INDUCED AXIONS

As we already mentioned the AQNs propagating in the Earth's atmosphere and interior will be losing their baryon charge as a result of annihilation processes. These processes will also lead to the axion emission as suggested in [19]. This new mechanism of axion production can be briefly explained as follows. The total energy of an AQN finds its equilibrium minimum when the axion domain wall contributes about 1/3 of its total mass [39]. This configuration in the equilibrium does not emit any axions due to a purely kinematical constraint: the static axion domain wall can be thought of as a superposition of off-shell non-propagating axions. However, this static picture drastically changes when some baryon charge from the AQN gets annihilated as a result of interaction with the environment when the time-dependent perturbations change this equilibrium configuration. In other words, the configuration becomes unstable with respect to the emission of the axions since the AQN is no longer at its minimum energy configuration with fewer baryon charges in the quark nugget core. As a result of these annihilation processes, the AQN starts to lose its mass, and consequentially the axion domain surrounding the quark matter wall starts to oscillate and shrink. These oscillations of the domain wall generate excitation modes and ultimately lead to radiation of the propagating axions. The spectrum of the corresponding AQN-induced axions

has been computed in [20].

Several important features of this spectrum deserve to be mentioned here. First of all, typical values $\langle v_{\text{axion}}^{\text{AQN}} \rangle \simeq 0.6c$ are very large in comparison with the conventional galactic non-relativistic axions $\langle v_{\text{axion}} \rangle \sim 10^{-3}c$. The corresponding Monte Carlo simulations have been carried out in [22], leading to the following estimate for the density of these relativistic axions on the Earth's surface:

$$\langle \rho_a^{\text{AQN}}(R_{\oplus}) \rangle \sim 5 \cdot 10^{-6} A(t) \frac{\text{GeV}}{\text{cm}^3}, \quad \langle v_a^{\text{AQN}}(R_{\oplus}) \rangle \simeq 0.6c, \quad (3)$$

where $A(t)$ is the modulation/amplification time-dependent factor. The factor A for the daily and annual modulations is discussed in the next Sect. IV below and is given by Eq. 6 and Eq. 7, correspondingly. In both cases, the factor A does not deviate from the average value $\langle A \rangle = 1$ by more than 10%.

However, one should emphasize that this normalization assumes the Standard Halo Model (SHM) DM distribution with $\rho_{\text{DM}} \approx 0.3 \text{ GeV} \cdot \text{cm}^{-3}$. The local DM density on the Earth's surface could be drastically different from this conventional value due to the capturing DM particles by the stars and planets, see e.g. [52] and refs therein. In fact, it was the main motivation of ref. [53] to critically analyse within the AQN framework the basic SHM assumption by performing some specific computations. In this and the next sections, we keep the conventional SHM value $\langle A \rangle = 1$ to avoid confusion with other effects that may modify the normalization $A(t)$ locally for a very short period of time (see also below).

The AQN-induced axions are mostly produced in the Earth's deep interior where the density of surrounding material is the highest. The energy density of the axions (Eq. 3) as well as the energy flux (Eq. 4) are not very sensitive to the axion mass m_a as explained in [22], in contrast with galactic non-relativistic axions assuming that DM is saturated by the galactic axions⁴.

It is instructive to compare the axion energy density (Eq. 3) of the relativistic axions with CMB photons because both components are relativistic particles. For the CMB photons, the energy density is well known and is given by $\rho_{\gamma} \approx 0.26 \text{ eV}/\text{cm}^3$, which is almost 4 orders of magnitude below the corresponding expression for AQN-induced axions on the Earth's surface (Eq. 3). The CaB axion density considered in [26] and mentioned in the Introduction must satisfy the condition $\rho_{\text{CaB}} \ll \rho_{\gamma}$. This implies that the density of the CaB axions must be at

least 4 orders of magnitude below the AQN-induced axions on the Earth's surface (Eq. 3).

There is a big difference in the distributions between the CMB photons and the axion energy density: the CMB photons are (almost) uniformly distributed over the entire Universe, while the axion density (Eq. 3) is localized around Earth and quickly vanishes at larger distances at $r \gg R_{\oplus}$. Similar estimates can be easily obtained for other stars and planets. Unfortunately, the axions do not couple with our visible material as strongly as CMB photons, which represents the major problem for their discovery despite their larger density (Eq. 3) in comparison with the CMB photons at the Earth's surface.

The resulting number density $n_a^{\text{AQN}} \simeq \rho_a^{\text{AQN}}/m_a$ is approximately 5 orders of magnitude smaller than the conventional galactic axion number density assuming that the galactic non-relativistic axions saturate the DM today. However, the flux ($v_a^{\text{AQN}} \cdot n_a^{\text{AQN}}$) related to relativistic axions (Eq. 3) is only 2 orders of magnitude smaller than the conventional flux of non-relativistic axion. Indeed, the AQN-induced axion energy flux on the Earth's surface can be estimated as follows [22]:

$$\langle E_a \cdot \Phi_a^{\text{AQN}} \rangle \simeq 10^{14} A(t) \left[\frac{\text{eV}}{\text{cm}^2 \cdot \text{s}} \right], \quad \langle E_a \rangle \simeq 1.3 m_a. \quad (4)$$

It is instructive to compare the AQN-related flux (Eq. 4) with the flux computed from the assumption that the galactic axions saturate the DM density $\rho_{\text{DM}} \sim 0.3 \text{ GeV} \cdot \text{cm}^{-3}$ today, see footnote 4. In this case, the numerical value for the flux (Eq. 4) is approximately two orders of magnitude below the value $10^{16} \text{ eV}/(\text{cm}^2 \cdot \text{s})$ computed for the conventional galactic non-relativistic axions assuming these axions saturate the DM density. One should emphasize once again that the density (Eq. 3) as well as the flux (Eq. 4) do not strongly depend on the axion mass m_a nor the initial misalignment angle θ_0 in contrast with conventional expression for the galactic axions, see footnote 4.

It is noted that the factor $A(t)$ could be numerically very large for a very short period in case of rare bursts-like events, the so-called ‘‘local flashes’’ in the terminology of Ref. [22]. These short bursts (with a duration time of the order of a second for $A \simeq 10^2$) result from the interaction of the AQN hitting the Earth in the close vicinity of a detector, see Tab. II.

Another important feature of the AQN-induced axions is the presence of the daily modulations, which is not a common feature of a generic DM model when a detector is not sensitive to the directionality, which is normally the case for most modern DM detectors. Rather, it is a very specific property of the AQN-induced production mechanism. The daily modulation plays a key role in our arguments. Therefore, we would like to explain the physical origin of this novel effect here.

The source of the daily modulation is the AQN's size difference between the moment of entry and moment of exit as a result of annihilation processes in the Earth's

⁴ The assumption on saturation of the DM density by the galactic axions cannot be satisfied in the entire window of $10^{-6} \text{ eV} \lesssim m_a \lesssim 10^{-3} \text{ eV}$ as the conventional contribution is highly sensitive to m_a as $\rho_a \sim m_a^{-7/6}$ and may saturate the DM density at $m_a \lesssim 10^{-5} \text{ eV}$, depending on additional assumptions on production mechanism. This, in particular, implies that for $m_a \gtrsim 10^{-4} \text{ eV}$ the conventional galactic axions contribute very little to Ω_{DM} , while the AQNs may be the dominant contributor to the DM density irrespective to the axion mass m_a .

TABLE II. Estimations of Local flashes for different A as defined by Eq. 4. The corresponding event rate and the time duration τ depend on the factor A , which is determined by the shortest distance from the nugget's trajectory to the detector. The table is adopted from [22]:

A	τ (time span)	event rate
1	10 s	0.3 min^{-1}
10	3 s	0.5 hr^{-1}
10^2	1 s	0.4 day^{-1}
10^3	0.3 s	5 yr^{-1}
10^4	0.1 s	0.2 yr^{-1}

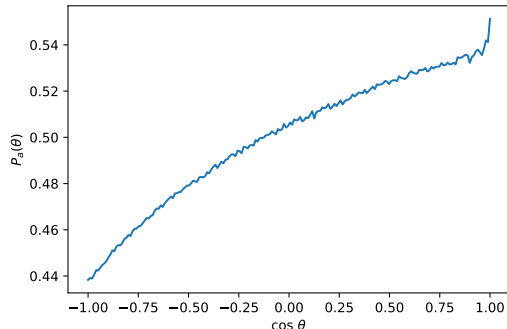


FIG. 1. The result of the Monte Carlo numerical simulations for the azimuthal distribution of axion flux $P_a(\theta)$ on the surface of the Earth, adopted from [22]. A relative orientation of the Earth's axis of rotation and DM galactic wind generates the flux asymmetry sensitive to the latitude θ , which consequently leads to the daily modulation effect.

interior⁵. Such effects do not exist for any fundamental particles such as WIMPs because the mass of any fundamental particle is the same at entry and exit points. The average size difference between the AQNs entering and exiting the Earth's surface may generate a large effect $\sim 10\%$ for the daily modulations as computed in [22] and explained below.

The key point here is the presence of relative orientation of the Earth's axis of rotation and the DM galactic wind. This relative orientation is an irrelevant parameter for conventional WIMPs if the detector is not designed to measure the directionality as already mentioned. For AQNs the flux is sensitive to this orientation. This effect eventually generates the flux asymmetry as a function of the latitude θ , which consequently leads to the daily modulation. This feature of the axion flux is expressed in terms of parameter $P_a(\theta)$ which is normalized to one, i.e. $\int P_a(\theta) \sin \theta d\theta = 1$. In the absence of the daily modulations parameter $P_a(\theta) = 0.5$ is independent of the lat-

itude θ . Our numerical Monte Carlo simulations shown in Fig. 1 unambiguously demonstrate the presence of the θ dependence, as explained above. This θ dependence generates the daily modulation.

The production rate of the low energy AQN-induced axions with $v_a \ll c$ is strongly suppressed as explained above. However, the axions that are produced with extremely low velocities $v_a \lesssim 11 \text{ km/s}$ will be trapped by the Earth's gravitational field. These axions will be orbiting the Earth indefinitely; therefore, they will be accumulated around the Earth during its lifetime of 4.5 billion years.

The corresponding Monte Carlo simulations have been performed in [21] with the following estimate for the gravitationally-bound axions:

$$\rho_a^{\text{bound}}(R_\oplus) \sim 10^{-4} \frac{\text{GeV}}{\text{cm}^3}, \quad \langle v_a(R_\oplus) \rangle \simeq 8 \frac{\text{km}}{\text{s}}. \quad (5)$$

The number density of the bound axions is at least 2 orders of magnitude smaller than conventional axion number density assuming that the galactic non-relativistic axions saturate the DM density. However, the corresponding wavelength $\lambda_a \sim \hbar/(m_a v_a)$ of the gravitationally bound axions is approximately 30 times greater than for galactic axions, which have a typical velocity of about $\sim 250 \text{ km/s}$. Therefore, coherent effects can be maintained for a longer time-period compared to those for conventional galactic axion searches. One may hope that the feature of having a large coherence length, $\lambda_a \sim v_a^{-1}$, could play a key role in the design of instruments, capable of discovering such gravitationally trapped axions.

One should also mention that these AQN-induced axions (relativistic as well as gravitationally bound) can be treated as a classical field because the number of the AQN-induced axions (Eq. 3) accommodated by a single de-Broglie volume is very large even though the de-Broglie wavelength λ for relativistic AQN-induced axions is much shorter than for galactic axions,

$$n_a^{\text{AQN}} \lambda^3 \sim \frac{\langle \rho_a^{\text{AQN}} \rangle}{m_a} \left(\frac{\hbar}{m_a v_a} \right)^3 \sim 10^6 \left(\frac{10^{-4} \text{eV}}{m_a} \right)^4 \gg 1.$$

IV. NEW STRATEGY: DETECTION OF BROADBAND AXIONS

The large average velocities $\langle v_a \rangle \simeq 0.6c$ of the emitted axions by AQNs change the entire strategy of axion searches since they are characterized by a broad distribution with $m_a \lesssim \omega_a \lesssim 1.8 m_a$ as discussed in the previous subsection. Therefore, the corresponding axion detectors must be some kind of broadband instrument. The cavity-type experiments such as ADMX are to date the only ones to probe the parameter space of the conventional QCD axions with $\langle v_a \rangle \sim 10^{-3}c$, while we are interested in the detection of the relativistic axions with $\langle v_a \rangle \sim 0.6c$. This requires a different type of instruments and drastically different search strategies. We assume that some

⁵ On average a typical nugget loses approximately 30% of its baryon charge when crosses the Earth. The axion domain wall shrinks correspondingly, which eventually generates the axion density (Eq. 3) at the Earth's surface from all AQNs transpassing the Earth's interior.

kind of broadband instruments can be designed and built, see reviews [14–18] with description of possible detectors.

With this assumption in mind, a new strategy to probe the QCD axion can be formulated as follows [23]. It has been known since [54] that the DM flux shows annual modulation due to the differences in relative orientations of the DM wind and the direction of the Earth’s motion around the Sun. The corresponding effect for AQN-induced axions was computed in [22]. The daily modulation which is a very specific feature of the AQN model, as explained in the previous section, was also computed in the same paper [22]. The broadband strategy is to separate a large frequency band into a number of smaller frequency bins with the width $\Delta\nu \sim \nu$ according to the axion dispersion relation as discussed above.

The time-dependent signal in each frequency bin $\Delta\nu_i$ has to be fitted according to the expected modulation pattern, daily, or annual. For example, the daily modulation should be fitted according to the following formula

$$\begin{aligned} \rho_a^{\text{AQN}}(t) &\equiv A_{(d)}(t) \langle \rho_a^{\text{AQN}}(R_\oplus) \rangle & (6) \\ A_{(d)}(t) &\equiv [1 + \kappa_{(d)} \cos(\Omega_d t - \phi_0)], \end{aligned}$$

where the density $\langle \rho_a^{\text{AQN}}(R_\oplus) \rangle$ is estimated according to Eq. 3. In this formula $\Omega_d = 2\pi \text{day}^{-1}$ is the angular frequency of the daily modulation, while ϕ_0 is the phase shift. It can be assumed to be constant on the scale of days. However, it slowly changes during the annual seasons due to the variation of the direction of DM wind with respect to the Earth. The modulation factor $A_{(d)}(t)$ is normalized to unity, $\langle A_{(d)}(t) \rangle = 1$ when one averages over a large number of daily cycles. The same modulation factor $A_{(d)}(t)$ with the same $\kappa_{(d)}$ also enters the estimation for the flux (Eq. 4).

A similar formula holds for the annual modulation defined as follows:

$$\begin{aligned} \rho_a^{\text{AQN}}(t) &\equiv A_{(a)}(t) \langle \rho_a^{\text{AQN}}(R_\oplus) \rangle & (7) \\ A_{(a)}(t) &\equiv [1 + \kappa_{(a)} \cos \Omega_a(t - t_0)], \end{aligned}$$

where $\Omega_a = 2\pi \text{yr}^{-1}$ is the angular frequency of the annual modulation and label “a” in Ω_a stands for annual. The $\Omega_a t_0$ is the phase shift corresponding to the maximum on June 1 and minimum on December 1 for the standard galactic DM distribution, see [54, 55].

Several tests can unambiguously discriminate a true genuine signal from spurious signals and noise. These tests will be discussed in detail in Sect. VB after some simplified estimates for the expected signal are performed in Sect. VA.

V. EXPECTED SIGNALS FROM THE AQN-INDUCED AXIONS

The goal of this section is twofold. First, in Sect. VA we want to highlight the basic differences in conversion rate between the AQN-induced relativistic axions and

the conventional galactic axions which normally enter the well-known formulae. Secondly, in Sect. VB we formulate the key element of this work: despite the very low rate of axion-photon conversion the daily modulation effect reviewed in the previous Sect. IV effectively allows us to discriminate the genuine signal from the spurious signals.

A. Estimates for the axion to photon conversion

The starting point for our analysis is the computation of the conversion rate which is determined by the well-known formula, see e.g. review [18]:

$$\begin{aligned} P_{a \rightarrow \gamma} &= \frac{1}{v_a} \left(\frac{gB}{q} \right)^2 \sin^2 \left(\frac{qL}{2} \right), & (8) \\ q &= \omega - \sqrt{\omega^2 - m_a^2} \end{aligned}$$

where L is a typical distance where the magnetic field B is present and $g \equiv g_{a\gamma\gamma}$ is defined as usual

$$g \simeq \frac{g_\gamma \alpha}{f_a \pi}, \quad g_\gamma = \frac{1}{2} \left(\frac{N_e}{N} - \frac{5}{3} - \frac{m_d - m_u}{m_u + m_d} \right) \quad (9)$$

where parameter $N_e/N = 0$ for KSVZ model, and $N_e/N = 8/3$ for DFSZ model such that $g_\gamma \approx -0.97$ for KSVZ model and $g_\gamma \approx 0.36$ for DFSZ model. The parameters f_a and m_a are not independent, but tightly linked in conventional QCD axion models:

$$m_a \approx 6 \cdot 10^{-4} \left(\frac{10^{10} \text{ GeV}}{f_a} \right) \text{ eV}. \quad (10)$$

In case of the resonant conversion when combination $(qL) \ll 1$ could be very small the conversion rate assumes the usual form $P_{a \rightarrow \gamma} = v_a^{-1} (gBL/2)^2$. The dependence $P_{a \rightarrow \gamma} \propto L^2$ should be interpreted as the presence of a coherent phenomenon when the amplitude of the transition is linearly proportional to the coherence length $\propto L$, while the probability $P_{a \rightarrow \gamma}$ shows the quadratic dependence $P_{a \rightarrow \gamma} \propto L^2$ as stated above.

For non-relativistic axions, which are normally assumed to be the case for haloscope studies, one can approximate $q \simeq m_a$. If one multiplies Eq. 8 with the axion flux $(\rho_a v_a)/m_a$ one arrives at the following expression for the flux Φ_γ which counts the number of microwave photons emerging from the magnetic field region per unit time and unit area:

$$\Phi_\gamma = \frac{(\rho_a v_a)}{m_a} P_{a \rightarrow \gamma} \approx \frac{\rho_a}{m_a} \left[\frac{gB}{m_a} \sin \left(\frac{m_a L}{2} \right) \right]^2. \quad (11)$$

This expression agrees with the formula of ref. [56] which was derived using a very different approach. It is important to note that Eq. 11 does not depend on the axion’s velocity v_a in the non-relativistic limit $v_a \rightarrow 0$. This is because Eq. 8 for the conversion is proportional to v_a^{-1} while computation of the Φ_γ requires multiplication of

the conversion $P_{a \rightarrow \gamma}$ to the axion flux which itself is proportional to v_a such that the dependence on v_a cancels out at small $v_a/c \ll 1$.

We now turn to our relativistic case for the AQN-induced axions. In this case, the axion density and the flux are determined by Eq. 3 and Eq. 4 correspondingly. Furthermore, the time formation of a photon is very short $\sim m_a^{-1}$. The corresponding length scale is determined by the De Broglie length $\lambda \sim m_a^{-1}$ which is also much shorter than the size of the system L . Therefore, the conversion process can be treated as it happens in an infinite volume system.

As a result, one can estimate the flux Φ_γ^{AQN} which counts the number of microwave photons emerging from the magnetic field region per unit time and unit area as a result of a *single* elementary process as follows:

$$\Phi_\gamma^{\text{AQN}} \approx \Phi_a^{\text{AQN}} P_{a \rightarrow \gamma} \approx \Phi_a^{\text{AQN}} \left[\frac{gB}{m_a} \sin\left(\frac{m_a L}{2}\right) \right]^2, \quad (12)$$

where we ignored all numerical factors of the order of one. In particular, we put for simplicity $\langle E_a \rangle \simeq m_a$, $\langle v_a^{\text{AQN}} \rangle \simeq 1$. We also ignore the complications related to the relative orientation of the magnetic field and axion momentum. We also ignore the differences between L_x, L_y, L_z characterizing the geometry of the magnetic field, etc. All these order of one effects can be ignored for our qualitative analysis in the present work. In principle, one should integrate over the axion spectrum computed previously with a specific geometry of the instrument when E_a approximately varies in the range $E_a \in (m_a - 1.8m_a)$. The non-resonant Primakoff conversion generates a complicated photon's broadband spectrum with $\nu \in (m_a - 1.8m_a)$. However, for our qualitative estimates when we want to study the parametrical dependence of the rate as a function of the key parameters such as the axion mass m_a , magnetic field B , the basic size of the detector L all these numerical factors of the order of one are irrelevant, and will be ignored in what follows.

Several key elements lead to the different treatments of the non-relativistic galactic axions in comparison with relativistic AQN-induced axions. First of all, the conventional treatment of the problem assumes the coherent conversion such that $P_{a \rightarrow \gamma} \propto L^2$ as explained above. This L^2 scaling holds as long as L is smaller than the De Broglie wavelength λ where conversion effectively occurs. If coherence persists up to distance $l < L$ the enhancement is much smaller, $L^2 \rightarrow Ll$ [18]. It should be contrasted with the AQN induced axions when $\Delta\nu/\nu \sim 1$ and one should average over many cycles such that $\sin^2(\frac{qL}{2}) \rightarrow 1/2$ in Eq. 12.

The second important element is as follows. Eq. 12 describes the conversion as a result of a *single* elementary process when a typical formation length is of order the Compton length m_a^{-1} . One should sum over the number of effective "layers" along the axion's path which is of order $(Lm_a) \gg 1$. This factor represents a strong enhancement factor. One should note that this factor $(Lm_a) \gg 1$

agrees with formula Ll presented in [18] when the coherence length l should be replaced to the Compton length, i.e. $l \rightarrow m_a^{-1}$.

Therefore, based on the above, we arrive at the following estimate for the total flux Φ_γ^{AQN} which counts the number of microwave photons emerging from the magnetic field region per unit time and unit area:

$$\Phi_\gamma^{\text{AQN}}(\text{tot.}) \approx \frac{A}{2} \Phi_a^{\text{AQN}} \cdot \left[\frac{gB}{m_a} \right]^2 \cdot (m_a L). \quad (13)$$

Numerically, this estimate can be presented as follows ⁶:

$$\Phi_\gamma^{\text{AQN}}(\text{tot.}) \approx 0.1A \left(\frac{g_\gamma}{0.97} \right)^2 \left(\frac{B}{10T} \right)^2 \left(\frac{L}{m} \right) \frac{\text{ph.}}{\text{m}^2 \text{day}}, \quad (14)$$

which implies that a detector with area $\sim 10 \text{ m}^2$ could see a few microwave photons a day. This rate, of course, is quite low. However, recent technological advances suggest that such photons can be, in principle, detected using e.g. single photon counters. We refer to a recent talk by Sonnenschein at the axion workshop [57] on broadband technology in axion searches.

What is important here is that this rate could get a significant boost for a short period of time when factor $A(t)$ could be much larger (than an average value $\langle A \rangle = 1$) resulting from the interaction of the AQN hitting the Earth in close vicinity of a detector, see Tab. II with the expected frequency of possible enhancements. For example, one should expect a daily burst with enhancement $A \sim 10^2$ which lasts for a second as shown in Tab. II. The rarer bursts are shorter in duration but could be much more powerful and pronounced.

Another point here is that the average rate is low, however, no detector tuning is required in contrast with conventional resonance-type experiments. Furthermore, as we already mentioned, the AQN-induced axion DM flux (Eq. 4) does not depend on the axion mass m_a in contrast with the conventional axion production mechanisms when $\rho_{\text{DM}} \sim m_a^{-7/6}$ (see footnote 4). As a result, the rate in Eq. 14 also does not depend on m_a and this holds for the entire allowed axion window $m_a \in (10^{-6} - 10^{-3}) \text{ eV}$.

The conversion rate in Eq. 8 allows us to estimate the excess of power due to the emitted microwave photons. First, we have to multiply the axion density (Eq. 3) by the conversion rate in Eq. 8. Secondly, one should average over many cycles such that $\sin^2(\frac{qL}{2}) \rightarrow 1/2$ and insert the enhancement factor $(Lm_a) \gg 1$ as explained after Eq. 12. Third, to estimate the released energy per unit of time one should divide the obtained expression to a typical formation time of the elementary process, $\Delta t \sim m_a^{-1}$. Collecting all these factors together we arrive at

⁶ We use the conversion factor for the magnetic field when Gauss $\approx 1.95 \cdot 10^{-2} \text{ eV}^2$ in Heaviside-Lorentz units when $\alpha^2 = e^2/(4\pi)$, see e.g. Appendix A in [18].

the following estimate for the power excess $P_\gamma^{\text{AQN}}(\text{tot.})$ due to the emitted microwave photons in unit volume:

$$P_\gamma^{\text{AQN}}(\text{tot.}) \approx A(t) \left(\frac{\langle \rho_a^{\text{AQN}} \rangle m_a}{2} \right) \left(\frac{gB}{m_a} \right)^2 (m_a L). \quad (15)$$

This estimate can also be represented in a conventional way as an excess of power in unit volume measured in W/m^3 :

$$P_\gamma^{\text{AQN}}(\text{tot}) \approx 10^{-26} A(t) \left(\frac{\text{Watt}}{\text{m}^3} \right) \left(\frac{g_\gamma}{0.97} \right)^2 \quad (16) \\ \times \left(\frac{B}{10 \text{ Tesla}} \right)^2 \left(\frac{L}{m} \right) \left(\frac{m_a}{10^{-4} \text{eV}} \right)^2.$$

This estimate can be compared with the conventional computations for the power excess P_a in cavity resonance-designed detectors when $P_a \propto 10^{-26} Q_\alpha (\text{W}/\text{m}^3)$, see [18] for a review. Numerically, the value presented in [18] is similar to our estimate (Eq. 16) though the conversion rates and the magnitudes for the axion densities of the AQN-induced and the galactic axions are very different. This numerical similarity will be used in what follows for illustrative purposes in our comparisons of the broadband strategy with conventional resonance-type searches.

The key element in resonance searches is the so-called “quality factor” $Q_\alpha \sim 10^6$ which increases the likelihood of the detection of the axion signal. Indeed, the power excess P_a in the conventional analysis is normally compared with the noise power P_{noise} such that the signal-to-noise ratio is determined by the formula

$$\frac{S}{N} \approx \frac{\sqrt{N} P_a}{P_{\text{noise}}} \approx \frac{P_a}{T} \sqrt{\frac{t}{\Delta\nu}}, \quad P_{\text{noise}} = T \Delta\nu, \quad N \approx t \Delta\nu$$

where T is the total system noise temperature, t is the integration time and the $\Delta\nu$ is the bandwidth of the axion signal. The “quality factor” $Q_\alpha \sim 10^6$ plays a crucial role in this approach. The basic idea here is to detect the narrow resonance line with $\Delta\nu \simeq 10^{-6} \nu$ with sufficiently long integration time by scanning each narrow frequency band to increase the signal-to-noise ratio.

However, the formula for the power excess $P_\gamma^{\text{AQN}}(\text{tot.})$, as given by Eq. 16, does not carry the enhancement factor $Q_\alpha \sim 10^6$ for the case of non-resonance conversion of the relativistic axions with $\Delta\nu \sim \nu$. Therefore, the entire logic of collecting the signal and discriminating it from the noise is very different from the conventional treatment of the cavity-type experiments briefly reviewed above. The key point for our studies is that there is a well-defined modulation factor $A(t)$ which allows us to discriminate the signal from the spurious events and noise by collecting the signal over entire frequency bands instead of scanning in a single narrow frequency band in cavity-type experiments. In particular, one should expect the daily modulation as discussed in the previous section.

The absence of the quality factor $Q_\alpha \sim 10^6$ in Eq. 16 implies that the broadband search is not particularly sensitive to the axion mass, except for a basic normalization factor $\sim m_a^2$ resulted from a large number of “layers” along the path of the relativistic axion, as explained above. This should be contrasted with conventional resonance type searches when the cavity is designed to be highly sensitive to a very specific narrow frequency band expressed in terms of Q_α . This feature (absence of the resonance sensitivity to m_a) is of course a direct manifestation of the non-resonance axion-photon conversion in the magnetic field when the resonance features of the cavity do not manifest themselves in expression for the power excess as given by Eq. 16.

Therefore, the only option we are aware of to determine the axion mass m_a in the broadband setting is to determine the frequency of a single photon recorded by a non-resonant axion photon converter. As mentioned after Eq. 14 such technologies that could detect a single photon in this frequency band may indeed become available soon.

We would like to illustrate the arguments presented above with the following numerical estimates. In conventional resonance type searches the factor $N \approx t \Delta\nu \approx 10^5$ for $\Delta\nu \simeq 10^{-6} \nu$ and $\nu \sim 1 \text{ GHz}$ such that $\delta P_{\text{noise}} \approx P_{\text{noise}} / \sqrt{N} \approx 0.3 \cdot 10^{-2} P_{\text{noise}}$ for $t \approx 1 \text{ min}$ which is a typical integration time in resonance searches.

It should be contrasted with broadband strategy when one collects a signal in the entire frequency band $\Delta\nu \sim \nu \sim 1 \text{ GHz}$ during the entire year (separately for each hour during the day). In this case the integration time $t \approx 10^6 \text{ s}$ and $N \approx t \Delta\nu \approx 10^{15}$ which is more than sufficient to overcome the absence of the quality factor Q in the broadband Eq. 13, Eq. 15, and Eq. 16.

There are a few additional important elements that may increase the likelihood of the axion discovery expressed in terms of parameter $A(t)$ which could be several orders of magnitude larger than its average value for a very short period. Furthermore, the estimates in Eq. 13 and Eq. 15 explicitly show the presence of enhancement factor $(L m_a) \gg 1$ which counts the number of “layers” along the relativistic axion’s path, which is a very distinct element in comparison with conventional searches for non-relativistic axions. This feature implies that if an instrument is asymmetric, e.g. $L_x \gg L_y$ it automatically becomes sensitive to the direction of the axion’s momentum, i.e. the instrument potentially becomes directionally sensitive to the AQN-induced axion flux. Therefore, potentially such an instrument allows us to study the DM distribution locally, in our galaxy beyond the conventional Standard Halo Model (SHM) paradigm. A hope is that these novel elements in data analysis can overcome the absence of large numerical factor $Q_\alpha \sim 10^6$ which is normally present in the cavity resonance type studies.

B. The reasoning behind the expected daily modulation

Now we turn our attention to the key element of the proposal of this work. AQN-induced axions manifest themselves with the systematic effect of possible daily modulations as given by Eq. 6. This implies that the count of the emitted microwave photons as given by Eq. 14 or an excess of power as given by Eq. 16 can be accumulated during a long period of time (measured in years). The presence of a signal can be analyzed by fitting to the daily modulation Eq. 6 by summation over all days over the entire season during a specific hour and fitting the resulting power excess as a function of time (measured in hours) during 24 hours period. Any other observables generated by the axions such as induced currents or induced voltage in the pickup loop (overviewed in previous Sect. IV) must also show the same daily modulations irrespectively to a specific recording method of a signal as the expression for $A_{(d)}(t)$ given by Eq. 6 remains the same for all observables.

While the rate of emission (or excess of power) is very low the total number of events collected during several years could be sufficiently high to see the daily modulations if they are present in the data. What is more important is that the corresponding studies can easily discriminate a genuine signal from spurious signals and noise.

The simplest test for such discrimination is to check that the phase ϕ_0 in the fitting Eq. 6 does not stay the same during the year. Instead, it must slowly vary during the annual cycle. In particular, the phase ϕ_0 should assume the value $\phi_0 \simeq \pi$ for daily modulations for two opposite seasons (e.g. summer vs winter) when the maximum becomes the minimum and vice versa. This test, based on the comparison of the frequency dependence in daily and annual modulation data, obviously requires much longer observation time, measured in years. However, it is a highly nontrivial test because all systematic errors are vastly different for the daily and annual modulations.

Another simple test is to analyse the data sets with $B = 0$ T. The corresponding analysis for $B = 0$ must generate very different from $B \neq 0$ T results. The corresponding $B = 0$ T and $B \neq 0$ T results should be very different to discriminate a true genuine signal from noise.

The same daily modulations can be analysed by performing the Fourier transform, in which case one should see a single well-defined peak at $\Omega_d = 2\pi \text{ day}^{-1}$ with a large number of possible smaller peaks with randomly distributed frequencies representing the noise and spurious effects.

Repeating the same procedure of the Fourier transform at $B = 0$ should not generate a well-defined peak at $\Omega_d = 2\pi \text{ day}^{-1}$. Instead, the analysis of the $B = 0$ T data sets should generate a randomly distributed mountain range, rather than a well-defined single peak.

A more powerful test to exclude a spurious signal is

based on the idea of using some kind of network of synchronized instruments to study correlated signals, see the original papers [23, 53] for the details.

There may be many background systematic fluctuations (due to temperature fluctuations, tides, atmospheric phenomena, human-related activities, etc) that could mimic the daily modulations studied above. The corresponding spurious signals could be in principle discriminated from the genuine axion signals by analysing the sets with $B = 0$ and the sets at a different season to observe the phase shift ϕ_0 in the fitting Eq. 6. It is very hard to imagine that any spurious signals and noise could generate all the features similar to the AQN-induced axions described above.

Our previous comments essentially imply that the cavity-type experiments which are to date the only experiments to probe the particularly interesting region of parameter space corresponding to standard QCD axion models with $10^{-6} \text{ eV} \lesssim m_a \lesssim 10^{-3} \text{ eV}$, can be used to study the daily modulation as described above. These instruments can be viewed as non-resonance axion-photon converters in the background of a large magnetic field.

One should also add that any axion search instrument presently operating can, in principle, analyze the daily modulation along the lines described above. This might as well include all previously recorded data sets. In other words, such studies can be carried out by any haloscope irrespectively of the conventional searches based on resonance scanning as the basic idea is to combine entire data sets (let us say collected during a specific month when phase ϕ_0 from Eq. 6 can be assumed to be constant) for each given hour to see if the data show any daily modulation.

In the present work, we implement this idea by analyzing the data sets collected by the CAST-CAPP detector from Sept. 2019 to Jun. 2021. At this stage, it should be considered as a proof of principle demonstration.

VI. DATA ANALYSIS

CAST-CAPP is an axion haloscope that operated from Sept. 2019 to Jun. 2021 at CERN in Geneva, Switzerland. It consists of four tuneable $23 \times 25 \times 390$ mm rectangular cavities, each with a volume of $V = 224 \text{ cm}^3$ which were placed inside one of the two bores of CAST's superconducting dipole magnet of 8.8 T. CAST-CAPP introduced two novel mechanisms to increase its sensitivity to DM axions but also to transient events:

- The phase-matching technique combines the power outputs from the four identical cavities coherently to increase the SNR linearly with the number of cavities
- The state-of-the-art fast-tuning mechanism with a speed of 10 MHz/min and a resolution of 100 Hz, together with wideband electronics to allow for a

search for transient events such as axion streams and axion miniclusters.

CAST-CAPP acquired 172 days of data using both single and phase-matched cavities in data-taking conditions. The total covered frequency range extended from 4.77 GHz to 5.43 GHz covering a parameter phase space of ~ 660 MHz corresponding to axion masses between $19.74 \mu\text{eV}$ to $22.47 \mu\text{eV}$. This allowed CAST-CAPP to exclude axion-photon couplings for virialized galactic axions down to $g_{a\gamma\gamma} = 8 \times 10^{-14} \text{ GeV}^{-1}$ at 90% confidence level [58].

The design and the data-taking scheme of the CAST-CAPP experiment were not originally optimized for a search of daily modulated signals. However, the large acquired bandwidth of 5 MHz compared to the resonance width of about 200 kHz, together with the wide frequency range of 660 MHz, allows a first proof of principle demonstration of such a novel analysis procedure.

A. Simulation

The AQN signal search is simulated using artificially modulated signals incorporated into simulated spectra. These spectra are composed of randomly generated noise superimposed onto authentic spectral baselines acquired from CAST-CAPP. The CAST-CAPP data are recorded in 1 min bins which are then converted into frequency-domain using a Fast Fourier Transformation (FFT). Each spectra carry a unique shape originating from the TE_{101} resonance mode of the cavities and the amplifier gain profile. To preserve this unique shape in the simulated spectra, we produce spectral baselines using a low-pass filter. Each simulated spectrum is comprised of artificial Nyquist noise multiplied by a randomly selected spectral baseline. The artificial noise has a Gaussian distribution of $\mu = 1$ and $\sigma = 1/\sqrt{\text{resolution bandwidth} \cdot \text{spectrum time length}} = 0.018$. Then, the artificial daily modulated signal is simulated using a sine function of tuned amplitude added on top of the artificial noise spectrum.

We performed multiple simulations with the data-taking time ranging from 1 day to 20 days at a single frequency and an AQN signal amplitude ranging from 0.01% to 3.5% of the mean spectral power. Fig 2 shows the combinations of simulation parameters i.e. number of data taking days and AQN amplitude percentage with respect to the mean spectral power on a 2D space while the color denotes if that specific combination yielded a significant signal that can be detected on a Lomb Scargle periodogram. The confidence level for the significance is set to be 90%. In Fig. 3, a periodogram for a significant AQN signal is shown for 5 days of data taking. In this case, the power of the AQN signal is adjusted to be 0.8% of the mean spectrum power.

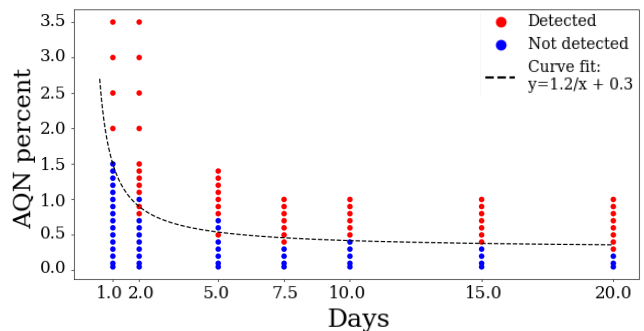


FIG. 2. Simulation of AQN signals with different power percentages as a function of data taking time. The red points indicate discoveries while the blue ones denote insignificant signals. A decision boundary fit is denoted by the black dashed line.

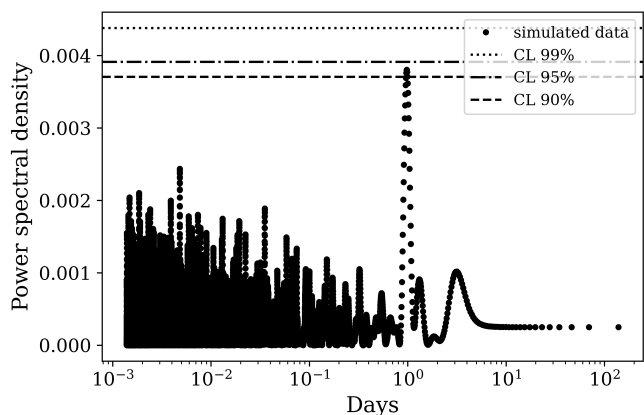


FIG. 3. Periodogram created using the Lomb Scargle method with 5 days of simulated data taking time (5 days / 1 min = 7200 simulated spectra). The observed signal is above 90% CL.

B. Data selection

During its ~ 2 years of operation, CAST-CAPP recorded 64.3 days of data using phase-matched cavities and 107.5 days of data using a single cavity. At the same time, a total of 16.4 days of data were recorded with $B = 0$ T. The total frequency range of CAST-CAPP is 644 MHz between 4.79 MHz to 5.43 MHz.

The strategy for quick identification of parasitic environmental background electromagnetic signals involved the usage of an external omnidirectional antenna that was placed outside the CAST magnet and was connected to a spectrum analyzer recording data simultaneously with the cavities. This EMI/EMC identification system was introduced in Nov. 2020 and collected 89.2 d of data.

For the search for a daily modulation with the CAST-CAPP data, only the data acquired from single cavities are used. The reason is that for the phase-matching procedure, a series of programmable phase-independent attenuators were used to adjust the amplitude of the res-

onance of the individual cavities with 0.25 dB to match the resonance peaks of the phase-matched cavities. This introduced additional attenuation although it is not expected to follow a daily rhythm, it could introduce unnecessary artifacts in the whole procedure.

Additionally, the data that were recorded during the usage of the fast-frequency scanning search approach are omitted from the analysis due to the inherent frequency-dependency of the amplitude of the resonance peak of the TE_{101} mode.

Therefore, as a first approximation only data taken from single cavities at fixed frequencies are used. Due to the high mechanical Q -factor of the sapphire strips of the tuning mechanisms, which were accidentally acting as a mechanical tuning fork, a frequency modulation of the electromagnetic mode of interest was observed in certain frequencies. The data that were dominated by such mechanical vibrations as well as other undesired non-systematic effects or possible EMI/EMC interferences were excluded from further consideration using a series of selection criteria.

C. Data treatment

Each CAST-CAPP spectrum that fulfills the aforementioned cuts is averaged within itself to get the mean spectral power, then a timestamp is attached to it. This way, a 2D array of mean spectral powers vs corresponding acquisition timestamps is created. This array is then rebinned hourly to have mean spectral powers for each hour of data acquisition.

The baseline on which the daily modulation in the CAST-CAPP data is investigated is expected to fluctuate due to weekly environmental temperature changes as well as amplifier gain drifts. To remove this effect before the daily modulation analysis, the data are detrended. For this purpose, a Savitzky Golay filter is used with a window length of two days and a polynomial order zero. Fig. 4 shows an example of the mean spectral power time-series belonging to cavity 3 between 13/08/2020 and 20/09/2020 with $B = 8.8$ T before and after the detrending procedure. The parameters of the low-pass filter are selected such that the long-range fluctuations are removed while the investigated daily variations are conserved. After detrending, the mean spectral variations are around a baseline that equals 1.

D. Systematics

CAST-CAPP's experimental setup consists of a three-stage signal amplification using HEMT amplifiers. The first amplification for each cavity was performed close to the critically coupled signal output port at the 4 K stage using a HEMPT low-noise amplifier (LNA) from Low Noise Factory (LNF-LNC4.8D) providing about 39 dB

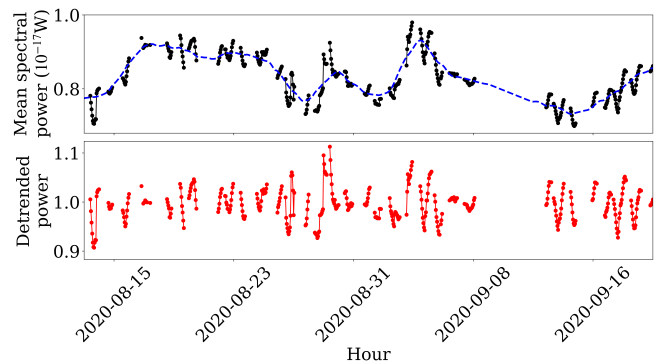


FIG. 4. Mean hourly spectral power (black) of cavity 3 between Aug 13 - Sep 20. The blue dashed curve denotes the trend of the data created by the low-pass filter. The detrended power (red) is calculated by dividing data (black) by its trend (blue).

amplification with 2 K noise for the frequency of CAST-CAPP at data-taking conditions. Then, an external amplification of about 22 dB for each of the four cavities is performed using four room-temperature ZX60-83LN-S+LNAs. Finally, a third stage amplification is performed at the output signal after the signal combination using a Miteq AFD3-0208-40-ST LNA providing about 30 dB gain.

Two main parameters that could influence the performance of these amplifiers are the provided bias voltage as well as the temperature. Regarding the bias voltage of the room-temperature amplifiers, this was provided using a Hameg HM7044 power supply. The accuracy of this power supply is on the level of 10 mV which translates into a tiny gain variation of about 0.007 dB or $\sim 0.2\%$ in terms of power for the second and third stage amplification. For the first stage amplification, a LNF-PS.3 was used for the biasing (0.25 V and 7 mA) for each one of the four LNAs corresponding to the four cavities. The biasing conditions of the LNAs were optimized for minimal heat dissipation and minimum noise figure. A current variation of about 0.02 mA was observed which would translate into a variation of the gain on the level of 0.02 dB or $\sim 0.5\%$ in terms of power.

The temperature of the first stage LNA was monitored through Cernox temperature sensors to be varied between 6 K to 10 K. For the specific bias of about 0.25 V and 7 mA at a frequency of ~ 5 GHz the gain of LNF-LNC4.8D has a linear dependency on temperature, increasing the gain of about 0.25 dB and an increase of their noise temperature 0.42 K for the aforementioned temperature range [59]. This translates into a $\sim 5.9\%$ variation of the gain in terms of power.

The temperature and humidity of the experimental area of CAST were monitored and kept stable via a central ventilation and temperature control system. However, small changes of a few degrees were observed. More specifically, the temperature variation observed in the

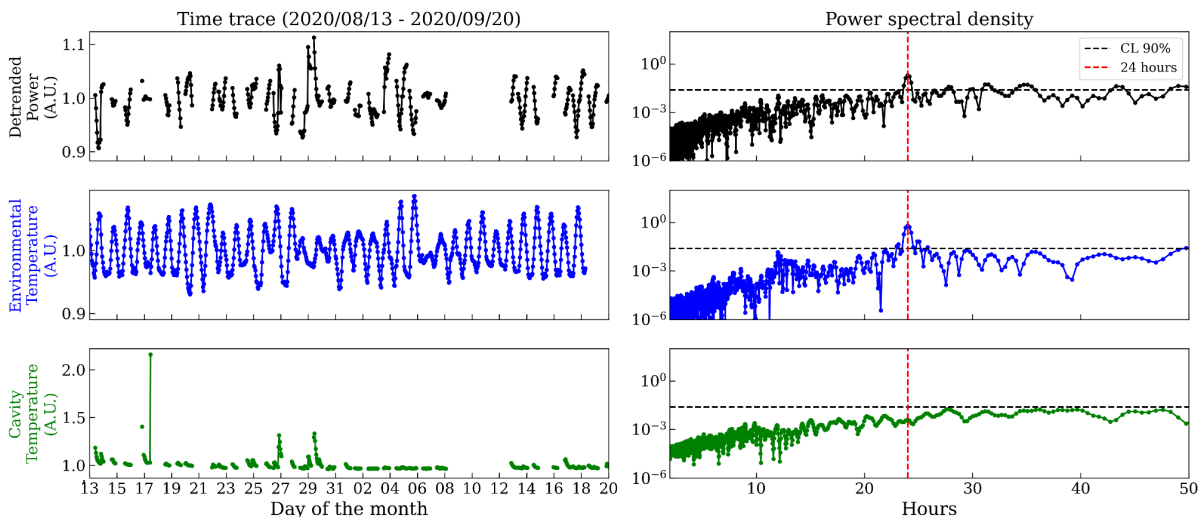


FIG. 5. Time series (left) and Lomb Scargle periodograms (right) for data taken between 13/08/2020 and 20/09/2020 with cavity 3 and $B = 8.8$ T. The results for the ambient environmental temperature as well as the cavity temperature are also shown.

room-temperature electronics of CAST-CAPP during the whole data-acquisition period was measured using PT100 RTD temperature sensors to be between 19°C to 26°C . These small temperature changes result in a linear gain dependency of the room-temperature amplifiers. For the second stage amplification a temperature change between 19°C to 26°C results in a decrease of the gain of about 0.078 dB or about 1.8% decrease in power [60]. Then, the third stage amplifier is expected also to have a decrease of its gain with increasing temperature of about 0.02 dB/ $^\circ\text{C}$ [61]. Therefore, for 19°C to 26°C , the third-stage room-temperature amplifier would exhibit a decrease of ~ 0.14 dB or about 3.3% decrease in terms of power.

It is noted that the gain stability of the amplifiers over time is expected to have a much smaller variation than the changes in temperature, voltage, or other ambient conditions. An overview of the aforementioned systematics and their effect on the gain of the various amplifiers of CAST-CAPP is shown in Tab. III.

	1 st stage	2 nd stage	3 rd stage
Temperature	+5.9%	-1.8%	-3.3%
Bias	-0.5%	+0.2%	+0.2%

TABLE III. Systematic effects on the variation of power from the various amplification stages of CAST-CAPP. The \pm signs indicate a positive or a negative correlation with the corresponding parameter.

Finally, the magnetic field of CAST’s dipole magnet was measured to have a stability of 0.1 mT at the level of 8.8 T, translating into an insignificant 0.001% variation.

E. Results

1. Lomb Scargle periodogram

The first step for a search for daily periodicities is performed using a Lomb Scargle periodogram in the detrended data. This way periodicities around 24 h can be investigated. Fig. 5 shows the time series (top left) as well as the periodogram (top right) for $B = 8.8$ T, where the time-period from 13/08/2020 to 20/09/2020 is selected for single cavity 3. At the same time, using the same period, the environmental temperature from the PT100 RTD temperature sensors (Fig. 5 middle row) as well as the cavity temperature from the Cernox sensors (Fig. 5 bottom row) are shown. Tab. IV gives a detailed account of the data statistics. The observed gaps in the time series for both the cavity power and the cavity temperature data are due to CAST-CAPP’s data acquisition scheme not being optimized for a daily modulation search, i.e. CAST-CAPP acquired single-cavity data for a limited and non-continuous amount of time. As the time series data were detrended and normalized, the y-axes are given in arbitrary units. In the periodograms (Fig. 5 right) that show the power spectral densities of the corresponding time series, the red dashed vertical line denotes the daily periodicity whereas the black dashed horizontal line shows the threshold for a significant signal with a confidence level of 90%.

As expected the environmental temperature follows a daily rhythm while the cavity, and therefore the cryogenic LNA temperature, does not. Interestingly, also the detrended cavity data for $B = 8.8$ T show a 24 h periodicity above 90% confidence level. However, the ambient temperature change can be the leading cause behind the observed daily variation due to its direct effect on the re-

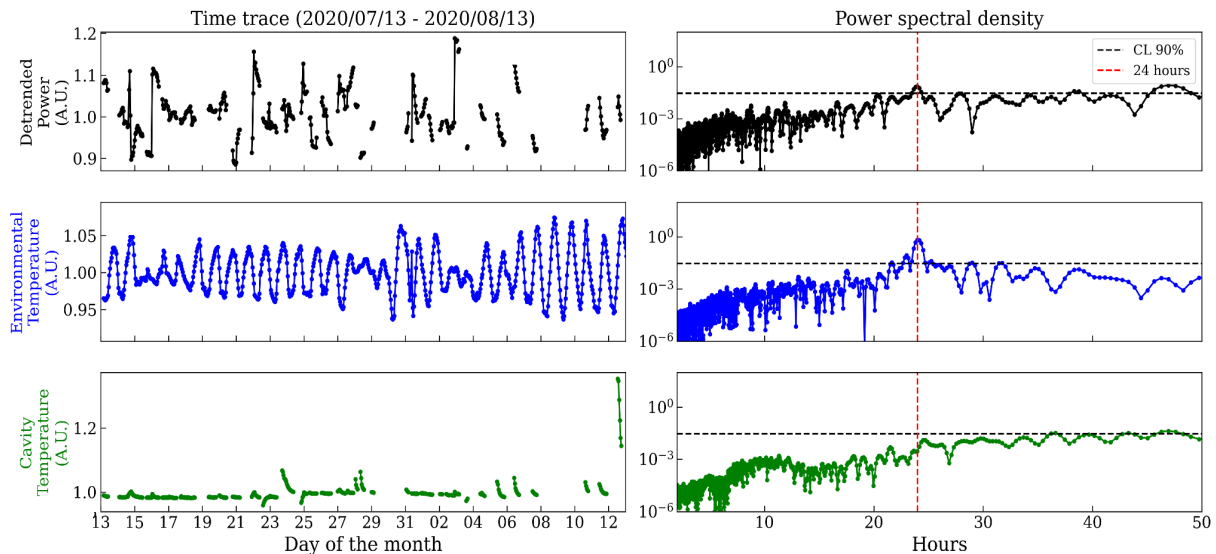


FIG. 6. Time series (left) and Lomb Scargle periodograms (right) for data taken between 13/07/2020 and 13/08/2020 with cavity 2 and $B = 0$ T. The results for the ambient environmental temperature as well as the cavity temperature are also shown.

	$B = 8.8$ T (Fig. 5)	$B = 0$ T (Fig. 6)
Interval	Aug 13 - Sep 20	Jul 13 - Aug 13
Data amount (1-min files)	14400	11500
Total hours	240	192
Hours per day	8.0	5.2
Frequency range [GHz]	5.20 - 5.33	5.32 - 5.41

TABLE IV. Data statistics for Fig. 5 and Fig. 6.

ceiver chain, as mentioned in the previous section. This is due to the room-temperature setup not being sufficiently isolated from temperature changes.

For comparison reasons also $B = 0$ T data are analyzed. For cavity 2, these are shown in Fig. 6 with the selected period ranging from 13/07/2020 to 13/08/2020. For practical reasons, this period could not be the same as the period for the $B = 8.8$ T, and therefore, a perfect comparison between the two can not be made. The time difference between the two is about 1 month. As can be seen, these data with $B = 0$ T also indicate a daily modulation being less pronounced than the $B = 8.8$ T data, which may be attributed to the $B = 0$ T data being more sparse compared to $B = 8.8$ T data. Therefore, we conclude that the appearance of similar daily modulation in the detrended power spectra of Figs. 5 ($B = 8.8$ T) and 6 ($B = 0$ T), does not allow to exclude systematics for the hint in Fig. 5 but strengthens the assumption of a temperature-dependent amplifier gain effect. Of course, there is always the possible dark photon contribution with no magnetic field dependence.

2. Hourly distributions

Next, the hourly distributions of both $B = 8.8$ T and $B = 0$ T data are shown in Fig. 7 which could provide more information on the observed daily modulation. These distributions are derived for the same time intervals as in Fig. 5 and Fig. 6, and are shown in the form of box plots in Fig. 7a, top and bottom, respectively. A sine function is then fitted to the data. The maxima of the fitted sinus shapes are found around 05:58 and 05:19 local hour, for $B = 8.8$ T and $B = 0$ T respectively.

Even assuming the sine-wave fit of $8.1\% \pm 0.6\%$ and $6.0\% \pm 0.5\%$ for the mean daily distributions of $B = 8.8$ T and $B = 0$ T respectively, the CAST-CAPP data do not allow for a significant conclusion in favor of the AQN-related axion signal.

The hourly temperature distributions corresponding to Fig. 7a are shown in Fig. 7b where we observe that the temperature is maximum at around 18:30 CET. This corresponds approximately to half a day phase shift between the mean spectral power and the ambient temperature variations shown in Fig. 5 and can be explained by the argumentation in Sect. VID.

Tab. V gives an overview of the sine fit characteristics for the box plots shown in Fig. 7. The sine fits, as shown by chi-squared tests, are significantly more suitable to the data compared to linear fits, confirming the daily periodicity observed. However, it is apparent that the daily change in the environmental temperature of the CAST hall does not allow for a positive conclusion.

Finally, as described in [58], an external quasi-omnidirectional antenna was placed next to the CAST magnet and operated simultaneously with the SA connected to the cavities and at the same frequency band.

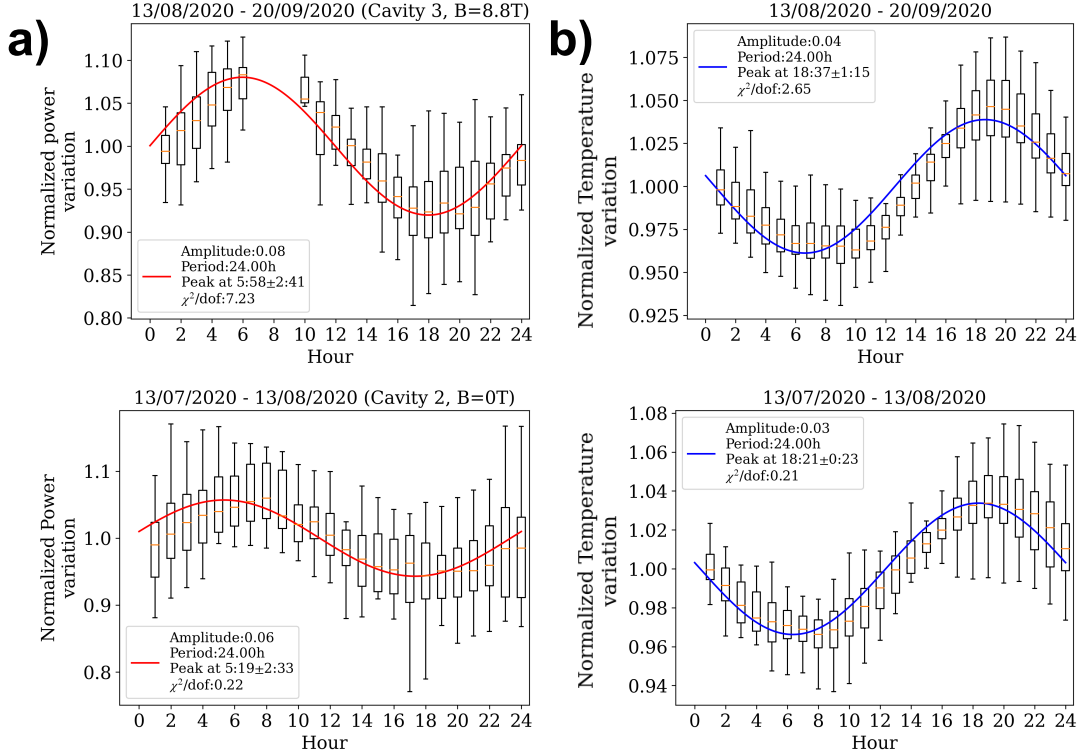


FIG. 7. Box plots showing the hourly distributions of the normalized power variation (left) and normalized environmental temperature variation (right) for $B = 8.8\text{ T}$ (top) and $B = 0\text{ T}$ (bottom). A sine function with a daily periodicity is fitted to the data. The gap in the upper left plot is due to the CAST-CAPP data acquisition schedule in that time interval of data taken.

		Cavity power	Environmental temperature
$B=8.8\text{ T}$	Fluctuation	$8.1\% \pm 0.6\%$	$3.7\% \pm 0.3\%$
	Max hour	$5:58 \pm 3:05\text{ CET}$	$18:37 \pm 1:15\text{ CET}$
	χ^2/dof	7.2(sine), 19.2(line)	2.6
$B=0\text{ T}$	Fluctuation	$6.0\% \pm 0.5\%$	$3.4\% \pm 0.3\%$
	Max hour	$5:19 \pm 2:33\text{ CET}$	$18:21 \pm 0:23\text{ CET}$
	χ^2/dof	0.2(sine), 8.3(line)	0.21

TABLE V. Data statistics for Fig. 7.

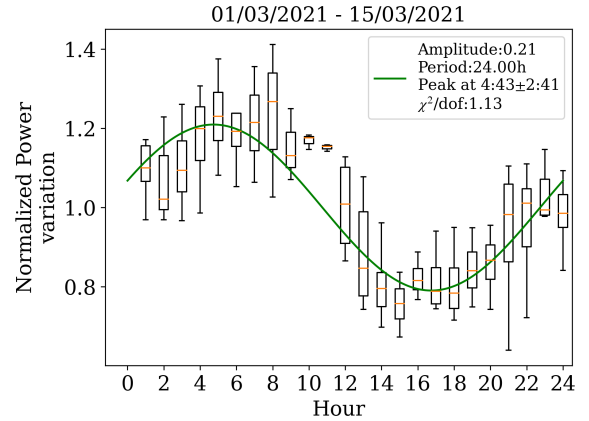


FIG. 8. Box plot of the external antenna spectral power.

This was used as a fast veto procedure where a candidate axion signal could be easily discarded if it appeared both in the cavities and in the witness channel at the same frequency. Therefore as an additional comparison, the hourly distribution of the external antenna data is shown in Fig. 8. As expected due to the lack of any temperature isolation, the mean daily spectral variation observed is about 21%, larger compared to both $B = 8.8\text{ T}$ and $B = 0\text{ T}$ data acquired by a receiver chain that is partially temperature isolated.

3. Seasonal phase shift

Due to the limited amount of data taken with CAST-CAPP, the expected seasonal phase shift (see Sect. VB) has been searched for, but it could not be conclusively identified. The periods 13/08/2020 - 20/09/2020 and 18/11/2020 - 02/12/2020 have been analyzed, where the expected phase shift is only of the order of 0.3π or 3

hours and 40 minutes, however, due to the limited statistics, this number could not be determined.

VII. CONCLUSION AND FUTURE STUDIES

In this work, as a proof of principle study, we have re-analyzed the CAST-CAPP data already published in [58], focusing on the daily modulation of a potential axion signal due to DM axions or from AQNs as it has been presented in Sect. V. We have observed daily variations, but at the same time also for $B = 0$ T (see Fig. 7 bottom) and with the external antenna (see Fig. 8). Since a similar dependence is expected for the electronic gain of the amplifier chain of the DAQ system, we could not conclusively determine an axion-related signal. Additional tests to discriminate a true genuine signal from the noise or spurious signals cannot be carried out as the CAST-CAPP detector is no longer operational. Thus, our measurements do not allow us to conclusively determine a DM axion signal (whatever its origin: from streams or AQNs), or a signal from the hidden sector. Although the data in Fig. 7 does show some daily oscillation, we conclude that this could be due to temperature effects. However, we can formulate some lessons to be learned which can be useful for future studies and different instruments, yet to be built.

The unavoidable fluctuations of the electronic gain of the amplifier chain, in radiometers, have led to the invention of the Dicke switch to eliminate such gain fluctuations of the entire chain, and not only the front-end like for the noise figure. The inherent switching noise added by this type of radiometer, can then be mitigated by the use of the correlation-type radiometer [62, 63]. Virtually every modern microwave remote-sensing satellite is based on this correlation technique, and therefore axion DM experiments can also benefit from this approach and replace the total power radiometer that is currently widely used. This approach can in the future allow for a conclusive search for daily modulations.

Additionally, the best option to discriminate the true genuine signal from the noise or spurious signals is to analyze the correlations in two or more different instruments representing a network, as suggested in [23, 53].

The basic idea is to search for some spikes that occur at (almost) the same instant in the different instruments of a network of axion detectors. The typical rate for such correlated events depends on the strength of the spikes as given in Tab. II.

Finally, to determine the mass and other parameters of the axion (assuming it is responsible for the daily modulation yet to be discovered) one should use a truly broadband instrument.

If future experiments conclude that the AQN-induced axions are responsible for daily modulation, it would have profound consequences. It would imply that two long-standing puzzles in cosmology, the nature of the DM and the matter-antimatter asymmetry of our Universe are simultaneously resolved. These two puzzles are intimately linked within the AQN framework and an observed signal cannot be explained by any other model since such a signal could be only generated by the relativistic AQN-induced axions (which are mostly localized on the Earth's surface in contrast with CaB⁷).

ACKNOWLEDGMENTS

This work has been supported by the Greek General Secretariat for Research Innovation (GSRI), the National Science and Engineering Research Council of Canada, the Institute for Basic Science (IBS) under Project Code No. IBS-R017-D1 of the Republic of Korea, the Spanish Agencia Estatal de Investigacion (AEI) and Fondo Europeo de Desarrollo Regional (FEDER) under project FPA-2016-76978-C3-2-P and PID2019-108122GB-C33, by the CERN Doctoral Studentship programme, the European Research Council (ERC), the DFG Research Training Group Programme 2044 “Mass and Symmetry after the Discovery of the Higgs Particle at LHC”, MSE (Croatia) and Natural Sciences and Engineering Research Council of Canada. We acknowledge support through the ERC under grant ERC2018-StG-802836 (AxScale project) and ERC-2017-AdG-788781 (IAXO+ project). Part of this work was performed under the auspices of the US Department of Energy by Lawrence Livermore National Laboratory under Contract No. DE-AC52-07NA27344.

⁷ As we mentioned in Sect. I the local density of the AQN-induced axions on the Earth's surface should be at least four orders of magnitude higher than the density of the cosmologically-produced CaB axions considered in [26], see paragraph above Eq. 4 for an estimate. This is because the CMB photon density strongly constrains CaB density. The spectral features of the AQN-induced axions are also vastly different from the CaB axions.

-
- [1] R. D. Peccei and H. R. Quinn, Constraints imposed by CP conservation in the presence of pseudoparticles, *Phys. Rev. D* **16**, 1791 (1977).
 - [2] S. Weinberg, A new light boson?, *Phys. Rev. Lett.* **40**, 223 (1978).
 - [3] F. Wilczek, Problem of strong P and T invariance in the presence of instantons, *Phys. Rev. Lett.* **40**, 279 (1978).
 - [4] J. E. Kim, Weak-interaction singlet and strong CP invariance, *Phys. Rev. Lett.* **43**, 103 (1979).
 - [5] M. A. Shifman, A. I. Vainshtein, and V. I. Zakharov, Can confinement ensure natural CP invariance of strong

- interactions?, *Nucl. Phys. B* **166**, 493 (1980).
- [6] M. Dine, W. Fischler, and M. Srednicki, A simple solution to the strong CP problem with a harmless axion, *Phys. Lett. B* **104**, 199 (1981).
- [7] A. R. Zhitnitsky, On Possible Suppression of the Axion Hadron Interactions. (In Russian), *Sov. J. Nucl. Phys.* **31**, 260 (1980), [*Yad. Fiz.*31,497(1980)].
- [8] K. Van Bibber and L. J. Rosenberg, Ultrasensitive Searches for the Axion, *Physics Today* **59**, 30 (2006).
- [9] S. J. Asztalos, L. J. Rosenberg, K. van Bibber, P. Sikivie, and K. Zioutas, Searches for Astrophysical and Cosmological Axions, *Annual Review of Nuclear and Particle Science* **56**, 293 (2006).
- [10] P. Sikivie, Axion Cosmology, in *Axions*, Lecture Notes in Physics, Berlin Springer Verlag, Vol. 741, edited by M. Kuster, G. Raffelt, and B. Beltrán (2008) p. 19, [astro-ph/0610440](#).
- [11] G. G. Raffelt, Astrophysical Axion Bounds, in *Axions*, Lecture Notes in Physics, Berlin Springer Verlag, Vol. 741, edited by M. Kuster, G. Raffelt, and B. Beltrán (2008) p. 51, [hep-ph/0611350](#).
- [12] P. Sikivie, Dark Matter Axions, *International Journal of Modern Physics A* **25**, 554 (2010), [arXiv:0909.0949 \[hep-ph\]](#).
- [13] L. J. Rosenberg, Dark-matter QCD-axion searches, *Proceedings of the National Academy of Science* **112**, 12278 (2015).
- [14] D. J. E. Marsh, Axion cosmology, *Phys. Rep.* **643**, 1 (2016), [arXiv:1510.07633](#).
- [15] P. W. Graham, I. G. Irastorza, S. K. Lamoreaux, A. Lindner, and K. A. van Bibber, Experimental Searches for the Axion and Axion-Like Particles, *Annual Review of Nuclear and Particle Science* **65**, 485 (2015), [arXiv:1602.00039 \[hep-ex\]](#).
- [16] R. Battesti *et al.*, High magnetic fields for fundamental physics, *Phys. Rept.* **765-766**, 1 (2018), [arXiv:1803.07547 \[physics.ins-det\]](#).
- [17] I. G. Irastorza and J. Redondo, New experimental approaches in the search for axion-like particles, *Prog. Part. Nucl. Phys.* **102**, 89 (2018), [arXiv:1801.08127 \[hep-ph\]](#).
- [18] P. Sikivie, Invisible Axion Search Methods, *Rev. Mod. Phys.* **93**, 015004 (2021), [arXiv:2003.02206 \[hep-ph\]](#).
- [19] H. Fischer, X. Liang, Y. Semertzidis, A. Zhitnitsky, and K. Zioutas, New mechanism producing axions in the AQN model and how the CAST can discover them, *Phys. Rev.* **D98**, 043013 (2018), [arXiv:1805.05184 \[hep-ph\]](#).
- [20] X. Liang and A. Zhitnitsky, Gravitationally bound axions and how one can discover them, *Phys. Rev.* **D99**, 023015 (2019), [arXiv:1810.00673 \[hep-ph\]](#).
- [21] K. Lawson, X. Liang, A. Mead, M. S. R. Siddiqui, L. Van Waerbeke, and A. Zhitnitsky, Gravitationally trapped axions on Earth, *Phys. Rev.* **D100**, 043531 (2019), [arXiv:1905.00022 \[astro-ph.CO\]](#).
- [22] X. Liang, A. Mead, M. S. R. Siddiqui, L. Van Waerbeke, and A. Zhitnitsky, Axion Quark Nugget Dark Matter: Time Modulations and Amplifications, *Phys. Rev. D* **101**, 043512 (2020), [arXiv:1908.04675 \[astro-ph.CO\]](#).
- [23] D. Budker, V. V. Flambaum, X. Liang, and A. Zhitnitsky, Axion Quark Nuggets and how a Global Network can discover them, *Phys. Rev. D* **101**, 043012 (2020), [arXiv:1909.09475 \[hep-ph\]](#).
- [24] A. R. Zhitnitsky, ‘Nonbaryonic’ dark matter as baryonic colour superconductor, *JCAP* **10**, 010 (2003), [hep-ph/0202161](#).
- [25] E. Witten, Cosmic Separation of Phases, *Phys. Rev.* **D30**, 272 (1984).
- [26] J. A. Dror, H. Murayama, and N. L. Rodd, Cosmic axion background, *Phys. Rev. D* **103**, 115004 (2021), [Erratum: *Phys.Rev.D* 106, 119902 (2022)], [arXiv:2101.09287 \[hep-ph\]](#).
- [27] T. Nitta *et al.* (ADMX), Search for a Dark-Matter-Induced Cosmic Axion Background with ADMX, *Phys. Rev. Lett.* **131**, 101002 (2023), [arXiv:2303.06282 \[hep-ex\]](#).
- [28] E. Farhi and R. L. Jaffe, Strange matter, *Phys. Rev. D* **30**, 2379 (1984).
- [29] A. De Rujula and S. L. Glashow, Nuclearites - A novel form of cosmic radiation, *Nature (London)* **312**, 734 (1984).
- [30] A. Zhitnitsky, Axion quark nuggets. Dark matter and matter-antimatter asymmetry: Theory, observations and future experiments, *Mod. Phys. Lett. A* **36**, 2130017 (2021), [arXiv:2105.08719 \[hep-ph\]](#).
- [31] A. Zhitnitsky, Cold dark matter as compact composite objects, *Phys. Rev.* **D74**, 043515 (2006), [arXiv:astro-ph/0603064 \[astro-ph\]](#).
- [32] V. V. Flambaum and A. R. Zhitnitsky, Primordial Lithium Puzzle and the Axion Quark Nugget Dark Matter Model, *Phys. Rev.* **D99**, 023517 (2019), [arXiv:1811.01965 \[hep-ph\]](#).
- [33] J. Singh Sidhu, R. J. Scherrer, and G. Starkman, Antimatter as Macroscopic Dark Matter, *Phys. Lett. B* **807**, 135574 (2020), [arXiv:2006.01200 \[astro-ph.CO\]](#).
- [34] O. P. Santillán and A. Morano, Neutrino emission and initial evolution of axionic quark nuggets, *Phys. Rev. D* **104**, 083530 (2021), [arXiv:2011.06747 \[hep-ph\]](#).
- [35] K. Lawson and A. R. Zhitnitsky, The 21cm Absorption Line and Axion Quark Nugget Dark Matter Model, *Phys. Dark Univ.* **24**, 100295 (2019), [arXiv:1804.07340 \[hep-ph\]](#).
- [36] S. Ge, K. Lawson, and A. Zhitnitsky, The Axion Quark Nugget Dark Matter Model: Size Distribution and Survival Pattern, *Phys. Rev.* **D99**, 116017 (2019), [arXiv:1903.05090 \[hep-ph\]](#).
- [37] X. Liang and A. Zhitnitsky, Axion field and the quark nugget’s formation at the QCD phase transition, *Phys. Rev. D* **94**, 083502 (2016), [arXiv:1606.00435 \[hep-ph\]](#).
- [38] S. Ge, X. Liang, and A. Zhitnitsky, Cosmological C P -odd axion field as the coherent Berry’s phase of the Universe, *Phys. Rev. D* **96**, 063514 (2017), [arXiv:1702.04354 \[hep-ph\]](#).
- [39] S. Ge, X. Liang, and A. Zhitnitsky, Cosmological axion and a quark nugget dark matter model, *Phys. Rev. D* **97**, 043008 (2018), [arXiv:1711.06271 \[hep-ph\]](#).
- [40] D. M. Jacobs, G. D. Starkman, and B. W. Lynn, Macro Dark Matter, *Mon. Not. Roy. Astron. Soc.* **450**, 3418 (2015), [arXiv:1410.2236 \[astro-ph.CO\]](#).
- [41] P. Gorham, Antiquark nuggets as dark matter: New constraints and detection prospects, *Phys. Rev.* **D86**, 123005 (2012), [arXiv:1208.3697 \[astro-ph.CO\]](#).
- [42] S. Ge, M. S. R. Siddiqui, L. Van Waerbeke, and A. Zhitnitsky, Radio impulsive events in quiet solar corona and Axion Quark Nugget Dark Matter, *Phys. Rev.* **D102**, 123021 (2020), [arXiv:2009.00004 \[astro-ph.HE\]](#).
- [43] A. Zhitnitsky, The mysterious diffuse UV radiation and axion quark nugget dark matter model, *Phys. Lett. B* **828**, 137015 (2022), [arXiv:2110.05489 \[hep-ph\]](#).

- [44] K. Mattila and P. Väisänen, Extragalactic Background Light: Inventory of light throughout the cosmic history, *Contemp. Phys.* **60**, 23 (2019), [arXiv:1905.08825 \[astro-ph.GA\]](#).
- [45] R. A. Flores and J. R. Primack, Observational and Theoretical Constraints on Singular Dark Matter Halos, *APJL* **427**, L1 (1994), [arXiv:astro-ph/9402004 \[astro-ph\]](#).
- [46] B. Moore, Evidence against dissipation-less dark matter from observations of galaxy haloes, *Nature (London)* **370**, 629 (1994).
- [47] M. Boylan-Kolchin, J. S. Bullock, and M. Kaplinghat, Too big to fail? The puzzling darkness of massive Milky Way subhaloes, *Mon. Not. R. Astron. Soc.* **415**, L40 (2011), [arXiv:1103.0007 \[astro-ph.CO\]](#).
- [48] A. Zhitnitsky, Structure formation paradigm and axion quark nugget dark matter model, *Phys. Dark Univ.* **40**, 101217 (2023), [arXiv:2302.00010 \[hep-ph\]](#).
- [49] A. Zhitnitsky, Solar Extreme UV radiation and quark nugget dark matter model, *JCAP* **10**, 050 (2017), [arXiv:1707.03400 \[astro-ph.SR\]](#).
- [50] N. Raza, L. Van Waerbeke, and A. Zhitnitsky, Solar Corona Heating by the Axion Quark Nugget Dark Matter, *Phys. Rev. D* **98**, 103527 (2018), [arXiv:1805.01897 \[astro-ph.SR\]](#).
- [51] X. Liang and A. Zhitnitsky, ANITA anomalous events and axion quark nuggets, *Phys. Rev. D* **106**, 063022 (2022), [arXiv:2105.01668 \[hep-ph\]](#).
- [52] R. K. Leane and J. Smirnov, Floating dark matter in celestial bodies, *JCAP* **10**, 057, [arXiv:2209.09834 \[hep-ph\]](#).
- [53] X. Liang, E. Peshkov, L. Van Waerbeke, and A. Zhitnitsky, Proposed network to detect axion quark nugget dark matter, *Phys. Rev. D* **103**, 096001 (2021), [arXiv:2012.00765 \[hep-ph\]](#).
- [54] K. Freese, J. A. Frieman, and A. Gould, Signal Modulation in Cold Dark Matter Detection, *Phys. Rev.* **D37**, 3388 (1988).
- [55] K. Freese, M. Lisanti, and C. Savage, Colloquium: Annual modulation of dark matter, *Rev. Mod. Phys.* **85**, 1561 (2013), [arXiv:1209.3339 \[astro-ph.CO\]](#).
- [56] A. N. Ioannisian, N. Kazarian, A. J. Millar, and G. G. Raffelt, Axion-photon conversion caused by dielectric interfaces: quantum field calculation, *JCAP* **09**, 005, [arXiv:1707.00701 \[hep-ph\]](#).
- [57] A. Sonnenschein, Broadband axion searches with coaxial dish antennas, *Axions beyond Gen 2*, Seattle, January 2021 .
- [58] C. M. Adair *et al.*, Search for Dark Matter Axions with CAST-CAPP, *Nat. Commun.* **13**, 10.1038/s41467-022-33913-6 (2022).
- [59] Low Noise Factory, Private communication.
- [60] Mini Circuits, Private communication.
- [61] Narda-MITEQ, Private communication.
- [62] A. Tanner, J. Bosch-Lluis, and P. Kangaslahti, Applications of the pseudo-correlation microwave radiometer, in *IGARSS 2022 - 2022 IEEE International Geoscience and Remote Sensing Symposium* (2022) pp. 7241–7244.
- [63] A. Menon, M. D. Grady, and T. Weller, A generalized radiometer system equation that includes temperature-dependent system losses, in *2019 IEEE 20th Wireless and Microwave Technology Conference (WAMICON)* (2019) pp. 1–4.